In-situ X-ray tomographic monitoring of gypsum plaster setting

Jérôme Adrien, Sylvain Meille, Solene Tadier, Éric Maire, Layla Sasaki

In-situ X-Ray tomographic monitoring of plaster setting

Jérôme Adrien[1]*, Sylvain Meille[1], Solène Tadier[1], Eric Maire[1], Layla Sasaki[1]

[1] Université de Lyon, INSA-Lyon, MATEIS CNRS UMR5510, Villeurbanne, France

* corresponding author. Tel.: +33 4 72 43 63 81; fax: + 33 4 72 43 85 39.

E-mail address: jerome.adrien@insa-lyon.fr

Abstract

The first real time monitoring of plaster hydration using X-Ray tomography is reported in this paper. Dissolution of hemihydrate particles and formation of a network of gypsum needles can be observed in 3D. A 3D quantitative analysis based on the microstructure evolution allows the determination of the degree of reaction. In particular, the size of hemihydrate particles is shown to have an influence both on the hydration kinetics and on the final microstructure of the set plaster. This work paves the way to the understanding of the relationship between microstructure evolution, chemical degree of reaction and mechanical strength development for material processed through a setting reaction.

Keywords

Hydration (A), Kinetics (A), Microstructure (B), Particle size distribution (B), *in-situ* X-Ray tomography

1. Introduction

Plaster is one of the most ancient materials used for construction in the world, with evidence of its use over several thousands of years (traces of gypsum in ancient Egypt are often considered as the first example of its use). Plaster is still largely used for dry wall due to its low cost, low toxicity, low embodied energy and also to its lightweight, sound absorption and fire resistance.

Its production starts from the calcination of gypsum, calcium sulfate dihydrate ($CaSO_4.2H_2O$), at around 120-130°C. During calcination calcium sulfate dihydrate loses ¾ of its crystallization water and turns into calcium sulfate hemihydrate ($CaSO_4.0.5H_2O$) also referred to as plaster powder. Plaster is then prepared as a solid binder through a hydration reaction in water, with the dissolution of calcium sulfate hemihydrate (HH) and the precipitation of calcium sulfate dihydrate (DH), as shown in Eq. 1. “Plaster” usually refers to both the calcium sulfate hemihydrate and to the final set material, made of calcium sulfate dihydrate. It can be classified as a hydraulic binder and its hydration is usually considered as being well understood, involving only one chemical reaction and fully crystalline highly pure components.

$$CaSO_4.\frac{1}{2}H_2O+\frac{3}{2}H_2O \rightarrow CaSO_4.2H_2O \quad (1)$$

The driving force for this hydration reaction is the higher solubility of HH in water as compared to DH. This phenomenon has been described first by Lavoisier and Le Chatelier back in 1765 and 1887 respectively and is largely reviewed in the literature. Authors often consider three steps in the hydration of plaster: dissolution of calcium sulfate hemihydrate leading to a supersaturated solution with respect to gypsum, nucleation and growth of gypsum needles and final formation of a solid material by entanglement of gypsum needles with complete depletion of HH.

The water to plaster (W/P) ratio, *i.e.* the amount of water used to hydrate the HH powder, is always

well above the theoretical stoichiometric mass ratio of 0.186. This higher amount of water increases the fluidity of the paste, which becomes moldable. This also explains the high level of porosity in the final material obtained after complete drying of the excess water.

Monitoring and controlling the kinetics of the setting reaction are critical for industrial purposes and many studies can be found in the literature on the use of chemical additives to accelerate or to delay the setting time of plaster. During the setting process, the plaster evolves both from a chemical point of view (monitored by the degree of reaction) and from a mechanical point of view (from a liquid paste to a solid material). Therefore, both aspects have been thoroughly investigated. For instance, the monitoring of the hydration reaction can be carried out using a large number of techniques, the most popular being calorimetry [1] as the hydration reaction (Eq. 1) is exothermic. Additional methods are also used such as electrical conductimetry in diluted pastes [2], X-Ray diffraction [3] or nuclear magnetic resonance [4] to determine the rate of water consumed by the hydration reaction. Other analytical techniques can be used, such as differential thermal analysis or particle size analysis but they can only be implemented *ex-situ;* thus, they require to stop the reaction at different times, and demand one sample per studied time. Nevertheless, all these methods allow the determination of the degree of the hydration reaction.

On the other hand, the solidification of plaster can be monitored by the measurement of rheological and mechanical properties during setting, either with standard methods just like Vicat and Gilmore needles, knife setting time, or using rheometers. The evolution of the elastic modulus versus time can also be monitored by the measurement of ultrasound speed through the setting paste [5].

Some authors tried to link the degree of reaction and the development of strength, based on a description of the development of the microstructure at different times. Lewry and Willamson [1] suggested an evolution of the microstructure in three stages: firstly, development of a matrix of gypsum needles providing the initial strength, then relief of internal stresses caused by the built-up of pressure associated with needles growth and finally increase of strength due to water evaporation

after complete hydration.

The detailed description of the bonds formation between gypsum crystals is beyond the scope of our study, but it is admitted that the contact forces are highly dependent on the crystallographic orientation of the crystal faces in contact, as measured by atomic force microscopy [6,7].

The morphological description of the entanglement of gypsum crystals after hydration, as well as its structuring during the hydration phase, is critical as it directly controls the final strength of the material. The observation of the evolution of plaster microstructure with time is seldom described in the literature and mainly after having stopped the hydration at different times. The only study where the setting process has been monitored *in-situ* is, to the best of our knowledge, the work by Ridge [8] showing the growth of gypsum needles under an optical microscope. Lewry and Willamson carried out a *post-mortem* analysis based on scanning electron micrographies of fractured surfaces after having stopped the hydration at different stages. This allowed them to show the concomitant presence of partly solubilized HH particles and newly formed gypsum crystals [9]. This method is widely used to characterize the local organization of crystals due to its relative easiness and the high resolution one can reach. However, it is not possible to monitor *in-situ* the evolution of the microstructure during setting. Besides, the protocol used to stop the hydration might impact on the observed microstructure.

X-Ray tomography has a strong potential for the study of plaster hydration, the presence of water and solid ensuring a good contrast between the phases. Historically, the first scans of gypsum were acquired at high resolution using synchrotron source on a hydrated plaster [10]. Recent work was done on the *in-situ* mechanical loading of fully hydrated plaster in a X-Ray tomograph [11]. Only two studies deal with the use of X-Ray tomography during hydration of plaster [4,10]. In Bentz 2002 [10], 3D scans showed the concomitant existence of gypsum crystals and HH particles, but without any quantitative analysis. In Song 2009 [4], 3D scans with a voxel size of 3 µm of hydrating plaster were acquired after stopping the hydration reaction after 60 minutes. Pore volume distribution was analyzed but no specific analysis of the pore evolution with hydration time was

performed. One example of an *in-situ* monitoring of hydration was carried out on a cement paste [12]. The hydration was studied with X-Ray synchrotron tomography from 1 to 60 days, as the hydration kinetics is much slower than for gypsum. The resolution of the X-Ray device used in this study, even if as low as 0.7 µm, was a limitation to monitor the cement hydration as the calcium silicate hydrates controlling the strength are nanosized.

3D volumes with a voxel size of a few micrometers can be acquired and reconstructed in about 3 minutes on a lab scale apparatus thanks to recent development in microtomography. The present study focuses on the real time monitoring of plaster setting using X-Ray tomography, for the first time to the best of our knowledge. The volume of material studied here is sufficiently large to give an average behavior of the setting of a plaster paste, with a statistical number of HH particles dissolving and with fluidity typical of an industrial process. 3D quantitative volume analysis is reported and the influence of HH particle size on the setting process and on the final microstructure of plaster is investigated; the evolution of HH particle size versus hydration time is also examined.

2. Materials and methods

2.1. Plaster preparation

A beta calcium sulfate hemihydrate was used for this study, supplied in store retail, with purity above 96%. The hydration reaction was prepared using a W/P ratio of 0.72. In general, the powder was used as received. In order to understand the influence of the granulometry of the raw powder on the microstructure of the set plaster, some plaster samples were prepared with HH sieved powder (either between 63 and 40 µm or below 40 µm).

The time when the HH powder was put in contact with water is referred to as the initial time in the paper. HH and tap water, stored at 23°C, were mixed by hand for 3 minutes. For X-Ray tomography

observation, the paste was injected with a syringe into a drinking straw with a diameter of 3 mm, directly mounted on the X-Ray tomograph. Knowing that surfaces of the setting paste were not observed, it was assumed that the bulk of the sample remained saturated with respect to water during the time period required for the complete acquisition (1 h 44 min). Setting time was separately characterized on the remaining paste, which was not injected into the straw, by the knife setting time method: setting time was then defined as the time after which a cut made in the paste with a blade remained opened.

2.2. X-Ray tomography – *in-situ* setting of the plaster

The internal observation of the microstructure evolution during the plaster setting was carried out by means of X-Ray tomography using a vtomex device (GE Phoenix|X-Ray GmbH) equipped with a 160 kV nano-focus tube, a tungsten transmitting target, and a 1920 x 1536 pixel Varian detector – see [13] for more details. The X-Ray tube produces a polychromatic conical beam. The experiments were performed at a voltage of 80 kV and a current of 280 µA, with a voxel size of 2.5 μm^3. Due to the fast changes during hydration, the acquisition parameters were optimized in order to reduce the scan time. A continuous rotation was used and the integration time was 333 ms for each of the 600 projections acquired over 360°. These parameters resulted in measurement periods of 200 s for a complete scan. The first scan was acquired 13 minutes (800 s) after the initial time; these 800 s corresponded to the time needed to prepare the sample (600 s) and to perform the first acquisition (200 s). In total, plaster setting was monitored during 6200 s after the initial time. After this time period, no more modification in the microstructure could be noted. The sample was then dried outside of the tomograph at 45°C until constant weight was reached. It was re-scanned afterwards to observe the final set and dried microstructure. Because fast acquisition was no longer an issue, this last scan (denoted 24 h in the paper) was achieved with improved conditions *i.e.*, 900 projections and averaging of 3 images at each step angle.

For coding the absolute value of the attenuation coefficient of each voxel, 32 bits volumes were reconstructed from the projections. The reconstructed volumes were first subjected to a median filtering. Then, the different scans were spatially registered: each scan was aligned with respect to the previous one to better follow-up the evolution of the microstructure versus time.

2.3. X-Ray tomography – final microstructure

X-Ray tomography was also used to perform 3D analysis at very high resolution (0.4 μm^3 per voxel) of the final microstructure of small pieces of plaster once set *ex-situ* (~ 0.5 x 0.5 x 5 mm). Note that such a very small voxel size requires very much care in doing the tomographic acquisition. The tomograph used, different from the one used for the *in-situ* experiment, was designed by the company RX Solutions. This tomograph is equipped with a LaB_6 emission tip for the X-Ray source, which ensures that the actual spot size is physically smaller than 0.4 µm. The resolution is then not modified by geometric blur and that the voxel size is really close to 0.4 μm^3. The Hammamatsu X-Ray source was operated with a LaB_6 cathode at a voltage of 100 kV. The detector was a Hamamatsu CCD camera with a pixel size of 12 µm. Each scan consisted of 900 projections with an exposure time of 5 s and an averaging of 3 radiographs for each projection. The cone-beam XCT data were reconstructed by a filtered back projection Feldkamp-algorithm. The reconstructed data were processed and visualized with the public domain ImageJ / Fiji shareware [14,15].

High resolution tomography was also carried out after final hydration of HH powder sieved between 63 and 40 µm and below 40 µm to check for the differences in microstructure with the reference material, prepared from unsieved powder.

2.4. 3D volumes analysis and quantification

A quantitative analysis of the 3D volumes was also carried out. The analyzed volume was 1.5 mm^3 *i.e.*, sufficiently large to collect significant information about the setting process as it contained initially tens of thousands of HH particles larger than 5 µm. The voxel gray values distribution in this volume was recorded at different times ranging from 800 s to 6200 s, as well as after the drying of the plaster; the corresponding histograms were computed. In parallel, the absolute value of the attenuation coefficient of the different phases present in the setting material were determined from specific regions using the volumes where they were the most present i.e., on the first volume (acquired at 800 s) for HH particles and ionic solution and on the last volume (6200 s) for gypsum and trapped air.

In order to study the influence of the particle size of the HH reactant powder on dissolution kinetics, easy to recognize individual HH particles of different initial sizes were manually selected and the evolution of their thicknesses was followed with time. Note that HH particles were all connected at the first observation time, which complicated the quantitative image analysis since the morphology of the individual HH particles could not be measured easily. Therefore, their size was measured using a mathematical morphology operation named “granulometry” (see [16] for more details).

Also, about 70 HH particles ranging from below 10 µm up to 70 µm were manually selected and divided into 7 classes depending on their initial measurable thickness, referred to as T_{800} in this study. For each class, the average thickness over 10 particles was calculated and its evolution with hydration time was plotted.

A 3D rendering of HH particles in the initial paste and of large porosities after setting was also computed. A first algorithm was used to detect 3D clusters of connected voxels and to label each separate connected clusters. Morphological parameters of these labels were finally calculated (volume, position, …).

Last but not least, granulometry measurement were performed on image acquired at 2.5 μm^3 to

assess the mesopore distribution. This method was also applied on high resolution images to measure the thicknesses of both gypsum phase and micropores.

3. Results

3.1. *In-situ* qualitative observation of microstructural evolutions during setting

The evolution of plaster microstructure during setting was first qualitatively observed. Figure 1 shows a same tracked cross-section obtained from the reconstructed volumes at five different times and after complete setting and drying of the sample (indicated as 24 h). The quality of the reconstruction is obviously not perfect. This is because of the low signal to noise ratio due to the fast acquisition and also to the possible motion of the sample during the time required for a scan. The microstructure of the sample is however rather clearly distinguishable from these images.

In the first picture scanned after 800 seconds (corresponding to the very first acquisition after the initial time), HH rounded particles are clearly visible in white, surrounded by a phase consisting of an ionic solution and gypsum crystals nuclei (in dark gray). The gypsum nuclei could not be imaged at such a resolution. Two large entrapped air bubbles, in black, can also be observed as frequently noted in set plaster [17]. The different morphologies and gray levels observed for the distinct phases (HH, ionic solution, gypsum and air) allowed us to monitor the evolution of each phase separately during the setting of the material.

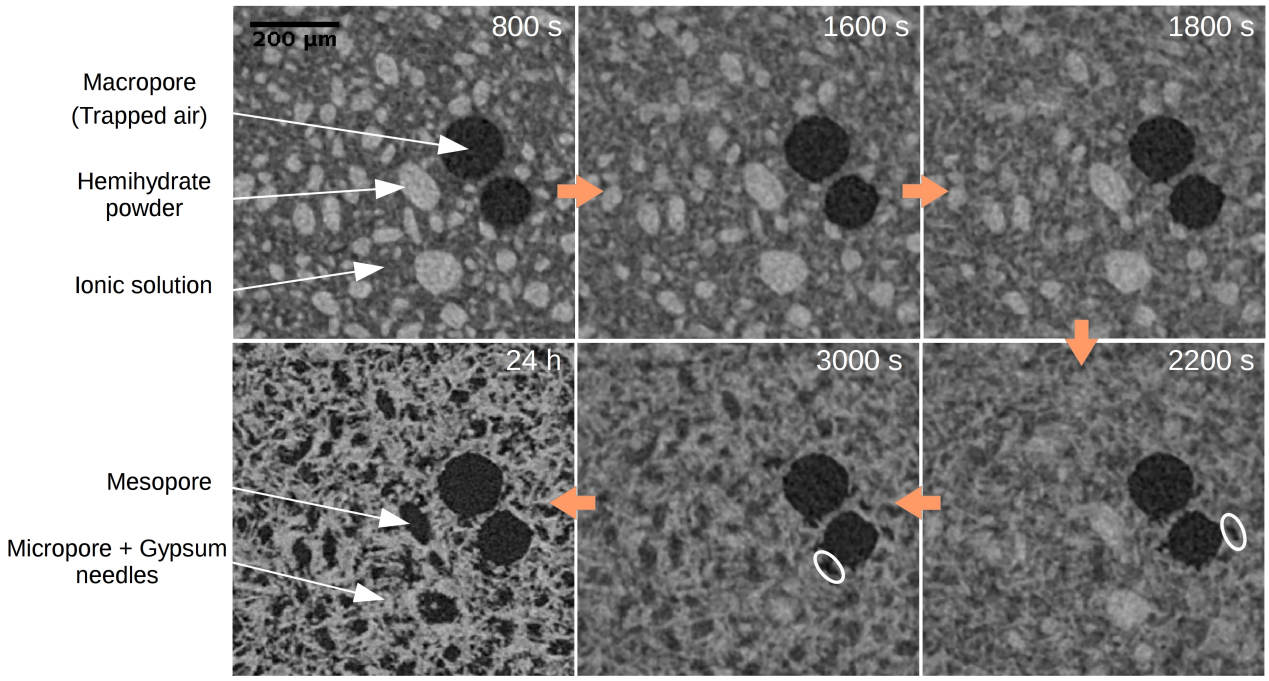

Fig. 1. Microstructural changes during the setting of plaster. Reconstructed 2D slices extracted from the 3D volumes acquired during the *in-situ* tomography experiments, between 800 and 3000 seconds. The last slice (24h) was obtained after drying at 45°C.

When considering the images shown in Figure 1 and the corresponding animated sequence (Video_1), modifications in the microstructure with setting time are evident. In particular, two phenomena are observable:

- the progressive dissolution of HH particles, with a visible influence of their size, the largest ones being the last ones to completely disappear,
- the formation of a network of gypsum needles inside the initial dark gray area i.e., inside the ionic solution (in terms of contrast, this leaded to a bleaching of the plaster matrix).

Both phenomena occurred in parallel, leading to a decrease of the gray level in the initial HH grain areas and to its increase in the zone initially occupied by the ionic solution. This indicates a clear transport of matter from the HH particles towards the solidifying crystals inside the ionic solution.

The entrapped air bubbles seemed unaffected by the setting reaction, despite a global reduction in size that will be quantified hereafter. One can also note that the desaturation of pores from ionic solution into air could be observed in the tomographic images: at 2200 and 3000 seconds, the pores located close to air bubbles (surrounded by a circle in Figure 1) started to have a darker gray level. As water absorbs X-Ray more than air, its gray value is higher compared to air. Therefore, the darkening of these pores clearly showed that they began to be filled with air rather than water, this phenomenon initiating from entrapped air bubbles.

The final microstructure obtained after drying (last image of Figure 1), acquired with the same voxel size but with improved imaging conditions, was typical of set gypsum, with an entanglement of gypsum crystals (in white) and three levels of porosity (in black):

- spherical macropores of several hundreds of microns were due to air bubbles entrapped inside the setting paste.
- irregularly shaped mesopores of several tens of microns (see arrows in Figure 1) were left by the dissolution of large HH particles,
- micropores formed a percolating network in the space left between entangled gypsum crystals.

With these experimental setting conditions, gypsum crystals have a typical average length of 15 µm and lateral dimensions between 1 and 2 µm [17]; therefore, they could not be individualized with the voxel size used here (2.5 μm^3). The comparison of the first and the final image highlights very clearly that the location of the final mesopores corresponded rather well to the position of initial large HH particles. Excepted for the air bubbles, the final microstructure (24 h) was nearly the exact negative of the initial one (800 s) in terms of attenuation coefficient.

Figure 2 shows the 3D rendering of a HH particle at 800 s and of the remaining mesoporosity after its complete dissolution. It confirmed that large HH particles led to the formation of mesoporosities. Morphological measurements were performed from the segmented volumes (cropped around the HH particle and the resulting mesopore) to calculate the respective dimensions of each object. The

results are summarized in Table 1: the mesopore was smaller and occupied only 52% of the initial HH particle volume, with an average uni-dimensional shrinkage of about 18%.

The same labeling measurements were performed separately on all trapped air bubbles. The results showed a limited volume decrease of approximately 8% between the first and the last acquisition and a negligible variation of the inter-bubble distance.

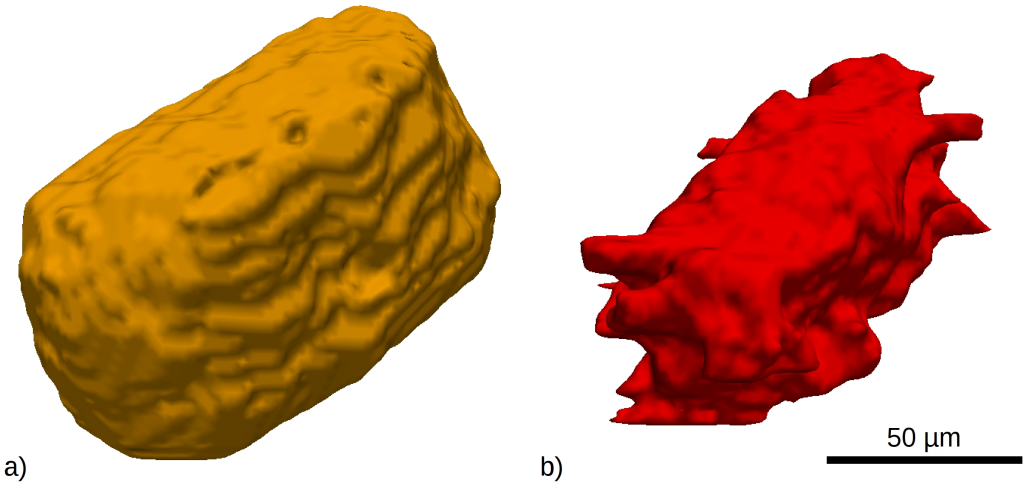

Fig. 2. 3D rendering of a) HH particle (800 s), length = 123 µm b) Resulting mesopore after setting and drying (24 h), length = 113 µm.

	Volume (µm^3)	A (µm)	B (µm)	C (µm)
Hemihydrate particle (HH) at 800 s	566 844	123	74	60
Mesopore (P) at 24 h	296 437	113	55	47
P/HH ratio	0.52	0.92	0.74	0.78

Table 1. Morphological parameters of the HH particle shown in Figure 2a and of the resulting mesoporosity (Figure 2b). A, B and C are the dimensions of the 3D objects in their three principal axes.

3.2. *In-situ* quantitative analysis of *dissolution / precipitation kinetics*

3.2.1. Global analysis – “microstructural” degree of reaction

As observed in Figure 1, the distinct phases (HH, ionic solution, gypsum and air) showed different gray levels. Therefore, in addition to a phenomenological description of the microstructure evolution during hydration, a quantitative analysis was carried out using 3D volume analysis. The characteristic gray level of each phase was determined: a typical gray value of 0.05 corresponded to trapped air (macropores), 0.15 to the ionic solution at 800 s, 0.21 to the matrix of growing gypsum crystals surrounded by the ionic solution and 0.31 to initial HH particles. The histogram of the voxel gray values distribution of the whole volume was computed at different times (Figure 3). At the beginning of the setting reaction, two peaks could be noted, corresponding to ionic water solution and to HH particles. During setting, these two peaks merged into a single one, which arose from the contribution of both the ionic solution and the growing gypsum crystals. The separation of these two phases could not be achieved because of the limited spatial resolution and of the small difference between the gray values of gypsum crystals and of the ionic solution. The gray value of the gypsum peak tended to increase during the setting process. After drying, this single peak separated into two peaks: one for gypsum, and one for air. Please note that imaging conditions were improved for the 24 h scan (dried plaster).

A degree of setting reaction was computed from the evolution of the intensity of the two peaks highlighted by dashed lines in Figure 3 i.e., the HH peak on the one hand and the gypsum peak on the other hand (Figure 4). Due to the setting reaction (Eq. 1), the intensity of the peak corresponding to HH decreased with time while the intensity of the gypsum peak increased. The evolution rate was not constant: after a slow evolution until 1000 s, the rate increased up to around 1600 s for HH dissolution and around 1800 s for DH precipitation. After 2500 s, no significant variations were observed anymore.

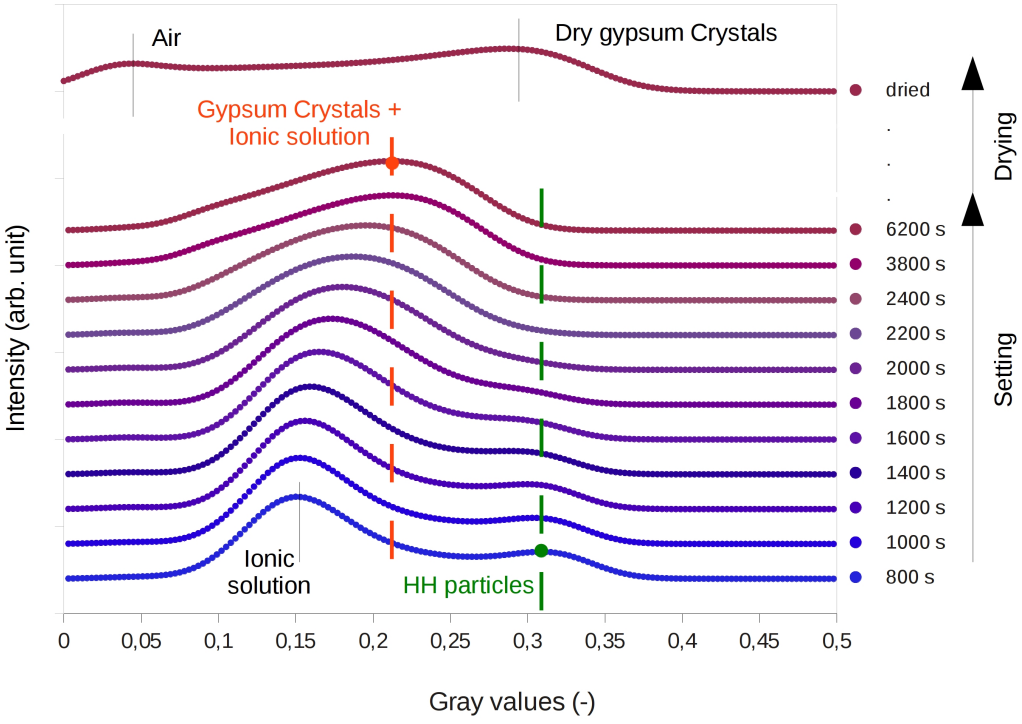

Fig. 3. Histograms of the gray values measured in the volumes for different times during setting and then subsequent drying at 45°C.

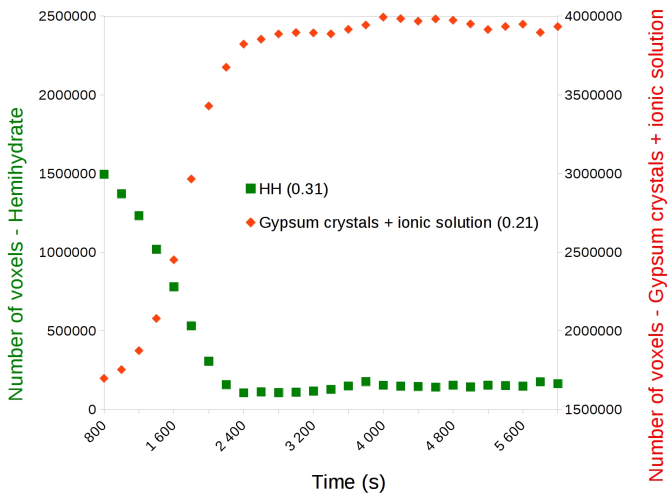

Fig. 4. Evolution of the intensity of the HH peak (dashed line in Figure 3, gray level value = 0.31) and of the gypsum peak (dashed line in Figure 3, gray level value = 0.21).

3.2.2. Local analysis - Influence of the HH particle size

As shown in Figure 1, the particle size of initial HH particles influenced their dissolution kinetics. To quantify this further, two single HH particles of different sizes were chosen and their dissolution was studied, by monitoring the evolution of the gray level profiles across the thickness of the particles with hydration time.

Figure 5 presents the evolution of the gray profile for a small HH particle, 20 µm thick, together with the corresponding micro-tomographies. At 800 s, the gray profile highlights the presence of a HH particle located between 11 and 38 µm (gray value above 0.3 typical of the HH phase, as shown previously), surrounded by the ionic solution, of characteristic gray values comprised between 0.15 and 0.18. For short times, nearly no evolution of this profile could be detected. Then the particle completely dissolved within a few minutes, between 1600 and 3200 s, leading to a mesoporosity filled with ionic solution (gray value around or below 0.1) surrounded by a shell made of gypsum crystals and microporosity, again filled with ionic solution. The profiles clearly showed, as already seen in Figure 1, that solid matter was progressively transported from the HH particle to the surrounding ionic solution where gypsum crystalline needles nucleated and grew, as confirmed by the increase of the gray level in the immediate vicinity of the initial HH particle.

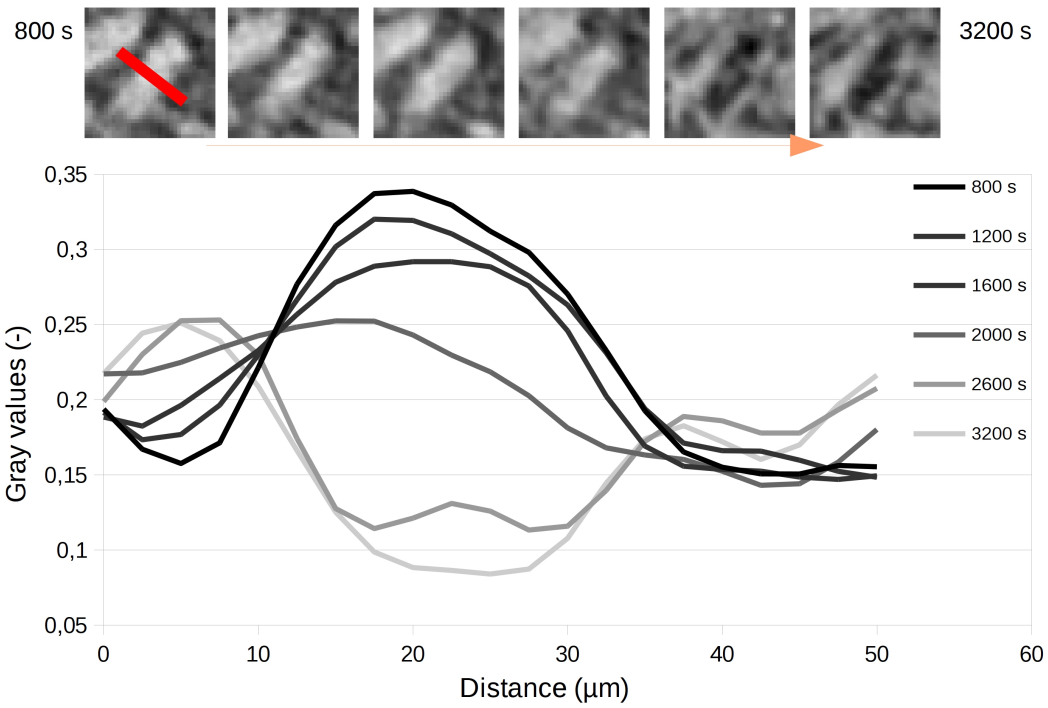

Fig. 5. Gray values profile along the red line taken at different setting times. The measurement was focused on a small HH particle (20 µm thick).

An example of the same analysis carried out on a large HH particle (approximately 70 µm thick), is illustrated in Figure 6. No evolution in the size of the particle was noted before the starting of dissolution at 1600 s. The dissolution suddenly started, occurring first at the surface of the particle. Again, the gray value of the area surrounding the HH particle increased during the dissolution of the particle: HH dissolved and matter was transported from the initial particle into the surrounding matrix where entangled needles of gypsum nucleated and grew. One can however note the existence of a shell of around 5 to 7 µm around the HH particle, where the gray value remained at 0.13 all along the dissolution, indicating that the HH particle was surrounded by a shell of ionic solution through which the matter had to diffuse towards the outside growing crystals. After complete dissolution, a remaining mesopore filled with ionic solution was left where the initial HH particle

was present. An outer shell made of a network of gypsum crystals and microporosity filled with ionic solution was observed. Figures 5 and 6 show that the behaviors of both small and large HH particles were very similar, excepted for the notable influence of the particle size on the dissolution kinetics. For the smallest HH particles present in the paste (below 20 µm in thickness), this phenomenon was probably too quick to be observed at our temporal resolution.

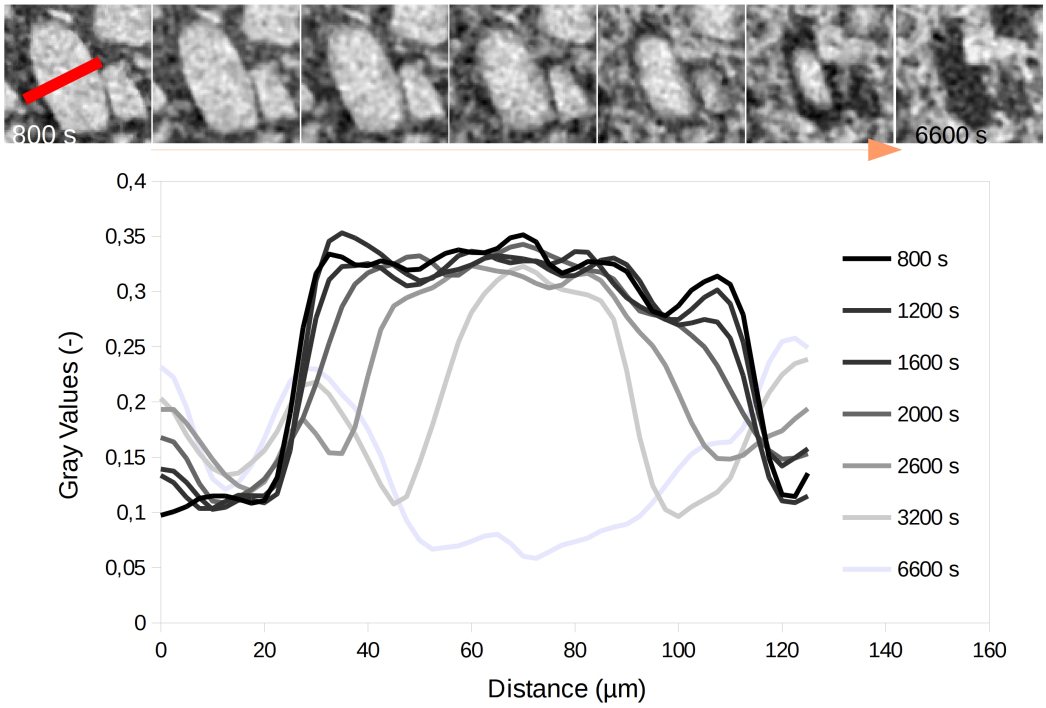

Fig. 6. Gray values profile along the red line taken at different setting times. The measurement was focused on a large HH particle (70 µm thick).

The evolution within time of the mean thickness of 70 different HH particles is presented in Figure 7a and confirms statistically the two individual cases discussed above. Even if, at 800 s, the dissolution had apparently already started for HH particles of size 20 µm and below, for most of the largest particles, dissolution had not yet started. Except for the smallest particles, an incubation time t_d could indeed be defined (intersection of the two tangent lines, see Figure 7a), during which the particle thickness remained rather constant. This time was computed for each size class of HH

particles and it was shown that t_d slightly increased with size, except for the largest HH particles, for which it was equal to 1820 s (Table 2). After t_d, the dissolution speed started to increase, slowly first, then reached a constant rate (steady state of dissolution) and finally decreased again just before the particles were fully dissolved. The linear part of the curve shown in Figure 7a could be used to compute the dissolution speed expressed as the change of the half-thickness versus time (dT/2dt). The calculated dissolution rates are collected in Table 2. For all particles above 50 µm, rates were all around 1.5 µm.min^{-1}. For HH particles of thicknesses below 40 µm, the dissolution speed decreased slightly with size. Note that this parameter was not calculated for the smallest particles (below 10 µm) because their dissolution had obviously started earlier than 800 s.

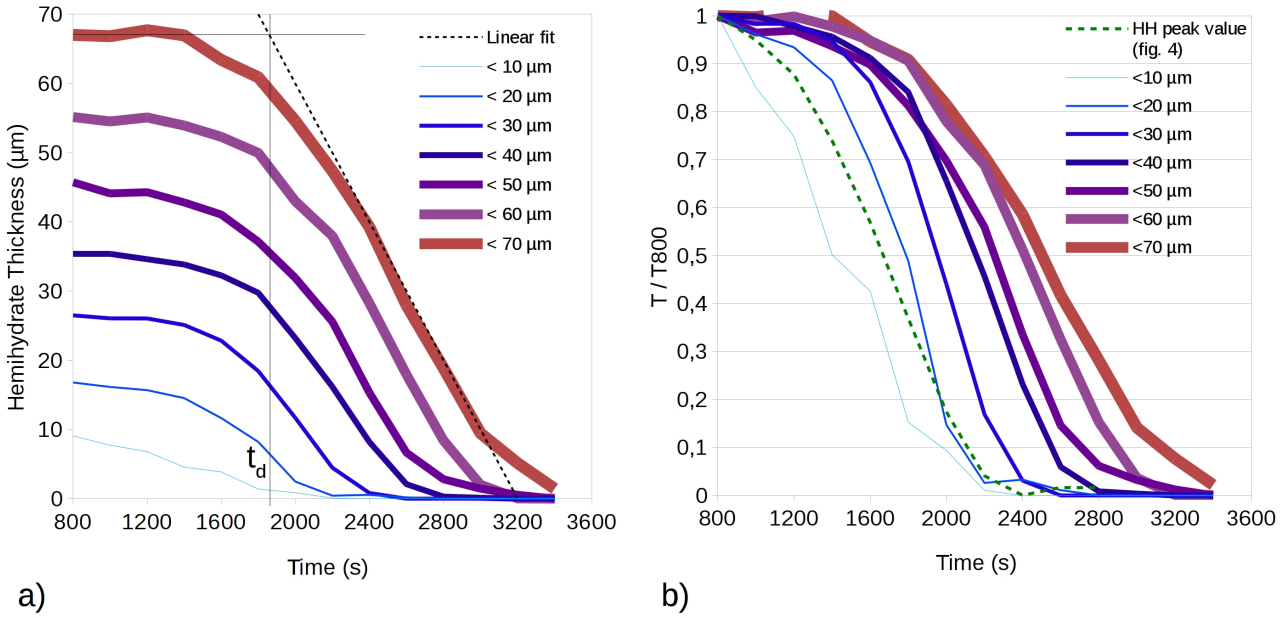

Fig. 7. a) HH thickness evolution during setting for different classes of initial particle sizes b) Normalized thickness evolution of HH particles (solid lines). The dashed line corresponds to the average HH dissolution throughout the whole volume as measured from data of Figure 4 (evolution of normalized intensity of HH gray value peak).

Initial HH particles thickness (µm)	< 20	< 30	< 40	< 50	< 60	< 70
dT/2dt in the steady state (µm.min^{-1})	0.84	1.08	1.14	1.44	1.5	1.5
Incubation time t_d (seconds)	1500	1600	1690	1780	1820	1820

Table 2. Dissolution speed of the HH particles in the steady state regime (linear fit from Figure 7a) and incubation time t_d for the different granulometric classes.

To be able to compare the dissolution kinetics of HH particles of different initial thicknesses, the dissolution curves plotted in Figure 7 were normalized: Figure 7b illustrates the evolution of T/T_{800} – thickness of the HH particle at a given time (denoted T) to its value at 800 s (denoted T_{800}) – for the different HH particle sizes. Also, the global HH dissolution curve shown in Figure 4 is reported in dashed line for comparison. It is close to the evolution of HH particles below 20 µm.

3.3. Quantitative observation of final microstructure - influence of HH particles granulometry

Set plasters obtained from the unsieved reference powder, and from HH powder sieved through two different mesh sizes (40 µm < HH particles < 63 µm and HH particles < 40 µm), were characterized after complete setting and drying. Slices of two reconstructed volumes with a voxel size of 2.5 µm^3 are presented in Figure 8a and b. Mesopores observed in the set plaster obtained after sieving of the HH powder below 40 µm (Figure 8b) were significantly smaller than mesopores of the reference material (Figure 8a). Besides, the global observation of the set material seems to reveal that the plaster obtained from the sieved HH powder was more homogeneous as compared to the reference plaster. We also noted the presence of a larger volume fraction of impurities (in white) in the sieved powder, the volume fraction of which was possibly increased during sieving.

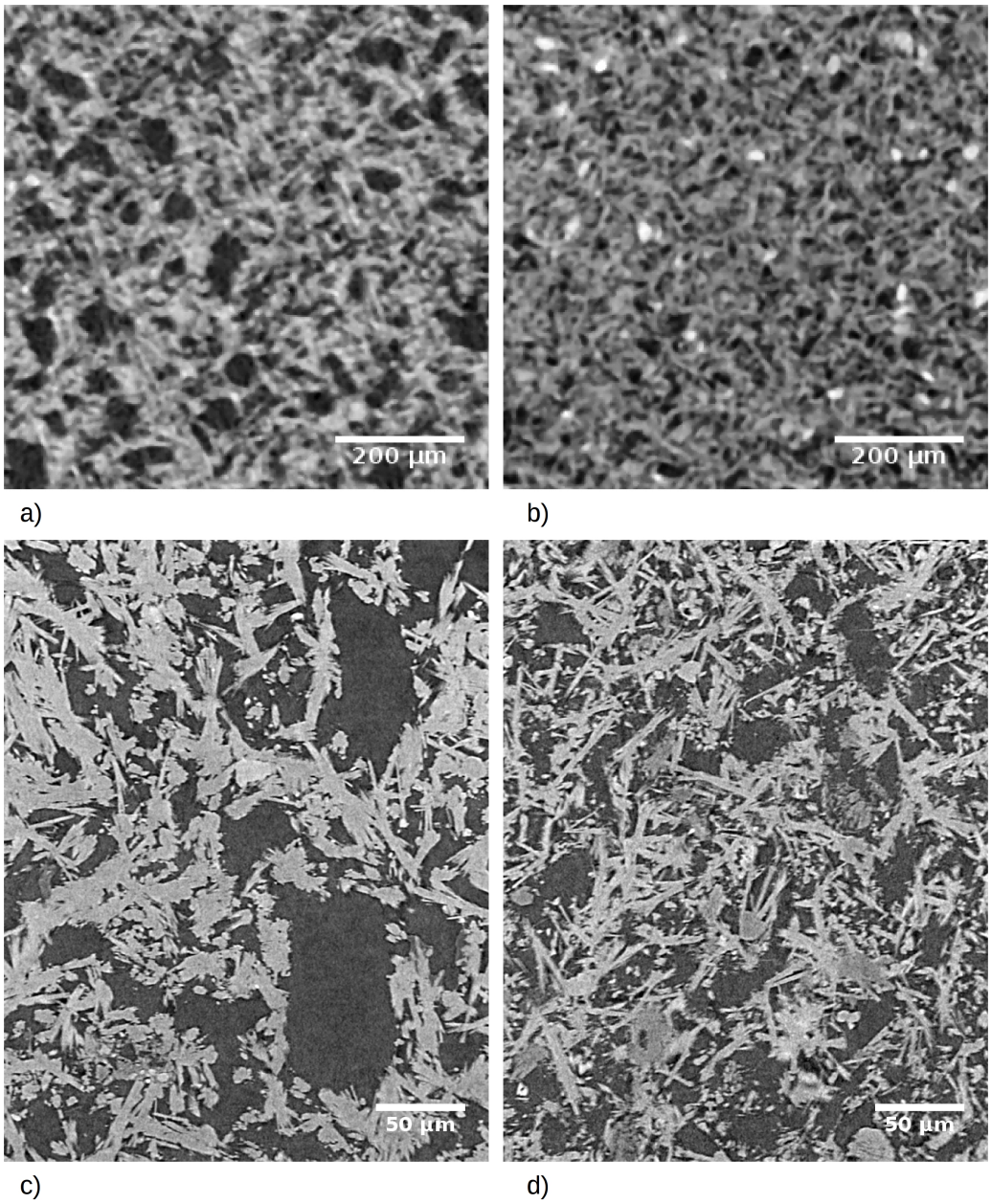

Fig. 8. Reconstructed 2D slices extracted from 3D volumes of set plaster samples obtained with a) the as-received HH powder and b) HH powder sieved below 40 µm – voxel size of 2.5 μm^3 and set plasters samples prepared with c) as-received powder and d) powder sieved below 40 µm – voxel size of 0.4 μm^3.

To better observe the influence of sieving the initial powder at a smaller scale, the microstructures of both set plasters shown in Figure 8a and b were also observed at a resolution of 0.4 μm^3 per voxel (Figure 8c and d). This confirmed the critical role of the large HH particles on the formation

of mesopores in the final material. For the sieved particles, the resulting gypsum network was more homogeneous, with numerous individual crystals and thinner bundles of crystals than in the reference plaster.

For quantification purposes, Figure 9 shows the mesopore size measured using the aforementioned granulometry technique from the tomographic scans of set plasters acquired with a voxel size of 2.5 μm^3 on volumes of $(1.25\ mm)^3$. Note that trapped air bubbles were easily excluded from the porosity analysis thanks to their much larger size (diameter > 80 µm) and spherical shape.

The results obtained confirmed the influence of the initial HH particle size on the mesoporosity size: the smaller the initial HH particles, the smaller the resulting mesopores. When HH particles below 63 µm were used, no mesopores larger than 50 µm were found and when HH particles below 40 µm were used, no mesopores larger than 40 µm were detected.

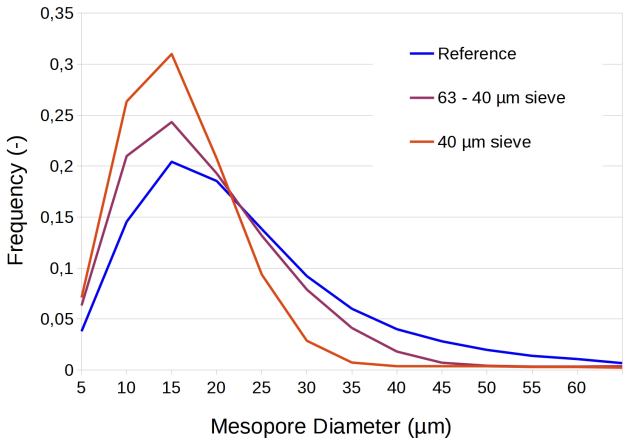

Fig. 9. Size distribution of mesopores in set plaster for different HH granulometry. « Reference » for sample prepared with as-received HH powder, « < 40 µm » for HH sieved below 40 µm.

Quantitative analysis of the granulometry of both solid and porous phases (including microporosity and mesoporosity) was also carried out on the tomographic scans of set plasters acquired at high

resolution (voxel size of 0.4 µm^3). Results are displayed in Figure 10. Data confirmed the finest microstructure generated by the sieved powder: interestingly, when the HH particles were sieved, not only the pore size was smaller but the gypsum crystals were also thinner and/or more individualized (as already shown in Figure 8).

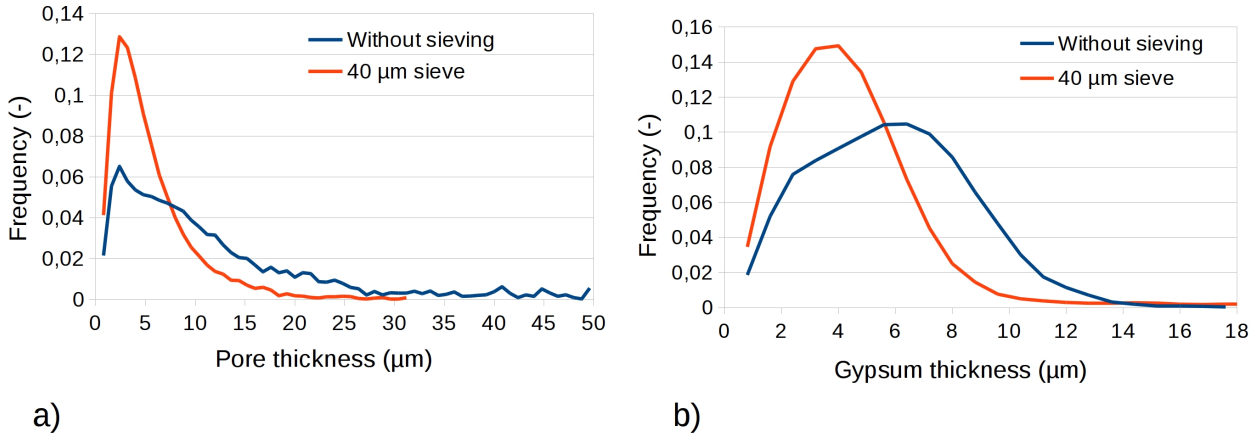

Fig. 10. Granulometry of the porous « phase » (a) and of the gypsum phase (b) measured from high resolution acquisitions (0.4 µm^3 voxel size).

The relative density of both set materials could be estimated by a simple count of the white pixels after image thresholding of the high resolution images. The relative density for the reference material was found to be 0.46 compared to 0.51 for the one obtained from the powder sieved below 40 µm, with an analyzed volume of 300 x 300 x 300 µm^3. As the W/P ratio was the same for the two materials, the final density should be exactly the same. The small difference noted could be due to an increase of impurities after sieving or by a more difficult control of the preparation of the sieved material, due to the limited amount of powder and to the higher surface to volume ratio of the sample, favoring water evaporation.

4. Discussion

The *in-situ* X-Ray tomographic observations during plaster setting and the quantitative analysis performed on the reconstructed volumes produced substantial information on the hydration process and on the resulting microstructure.

Figure 11 shows a schematic representation of the microstructural changes observed in Video 1 during plaster setting, starting from 800 s after the contact of HH powder with water (Figure 11a). No gypsum nuclei could be observed at this stage due to the limitation in spatial resolution. However, based on the results presented here, it can be assumed that some gypsum crystals were already formed. The dissolution of HH, beginning with the dissolution of the smallest HH particles, and the growth of dihydrate inside the surrounding ionic solution occurred simultaneously (Figure 11b). The formation of a network of gypsum needles was gradually observed (Figure 11c) while locally some large HH undissolved particles were still present confirming the observation by [9] and [10]. Although the limited resolution of the scanned volumes during hydration does not allow a direct observation of nucleation and growth of the gypsum crystals, it was clearly observed that gypsum crystals did not form at the surface of the initially large HH particles, and that an ionic shell permitting the transport of matter from the dissolving HH particles towards the growing crystals existed (Figure 11c). The observations showed that the dissolution process was not yet completed after 3000 s and that part of initially large HH particles still remained (Figure 11c). After setting, gypsum crystals were not observed where large HH particles were originally located (Figure 11d). The resulting mesopores had nevertheless a smallest size compared to the HH particles at 800 s (52% of the initial volume), due to gypsum precipitation in the outlying areas. This is clearly shown by the evolution of the gray values around HH particles between initial and final times in Figures 5 and 6.

It has also been noted that some mesopores located close to entrapped air bubbles began to be filled with air rather than ionic solution at the last step of hydration (starting from 2200 s in Figure 1).

562 This phenomenon probably arose from the consumption of water during the hydration equation of
563 HH particles (Eq. 1) inducing a desaturation of large pores. It is commonly encountered in Portland
564 cement pastes and associated to an important shrinkage due to the very small pore size of this
565 materials (few nanometers). In our study, the global volume variation of the plaster during setting,
566 measured via the distance between air bubbles, was negligible. The hydration reaction of gypsum is
567 accompanied with a 10 % volumetric shrinkage (usually referred to as Le Chatelier contraction),
568 often counterbalanced by an expansion during gypsum crystal growth [18] as it seems to be the case
569 in our study.
570 A decrease by 8% of the total volume of entrapped air was observed between the first and the last
571 volume acquired. Since the inter-bubble distance did not change during hydration, this could be
572 linked to the formation of gypsum crystals on the edges of trapped air bubble (Figure 11d).
573
574

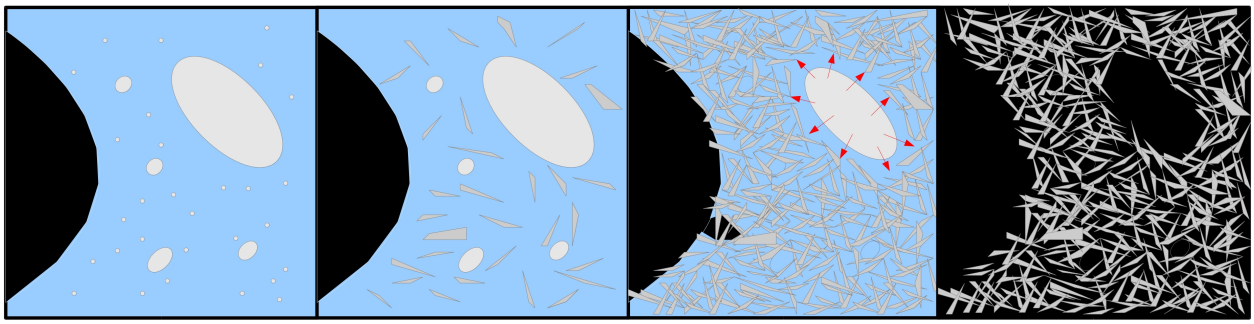

Fig. 11. Schematic representation of the hydration process as monitored by X-Ray tomographic observation (blue : water ; black : entrapped air ; white : HH particles of typical size between a few µm and tens of µm ; gray : DH crystals).

575
576
577 Quantitative analysis on the whole volume permitted to compute histograms of the gray values
578 measured at different times (Figure 3). A logical decrease of peaks associated to HH particles and
579 ionic solution was observed throughout the setting process (Eq. 1). A concomitant increase of the
580 peak associated to DH crystals was noted. During setting, this peak shifted towards higher gray

values due to gypsum precipitation and densification of the solid matrix. After drying, it showed an even stronger shift towards high values. The precipitation of gypsum during evaporation of the remaining water cannot explain such a strong shift. Indeed, a rapid calculation shows that, for the W/P ratio used here, the precipitation of crystals from the remaining ions would lead to a maximum 1 wt. ‰ increase of gypsum. Nevertheless, this last scan has been acquired in different conditions than the previous ones. In particular, the presence of water inside the paste during *in-situ* observations is known to have a potential detrimental effect on the images contrast (because of X-Ray beam scattering).

The microstructural degree of reaction highlighted two distinct regimes (Figure 4). Starting from 800 s, there was an acceleration followed by a slowing down of HH dissolution and DH precipitation until no more significant changes could be monitored. The times at maximum rates were slightly different for the two phenomena: DH precipitation was logically delayed compared to HH dissolution.

Regarding the influence of HH particle size, at 800 s, the smallest particles had already begun to dissolve whereas large particles seemed unaffected (Figure 7). It seems logical that the incubation time t_d increased with the HH particle thickness (Table 2), as smaller particles are more unstable due to their higher surface to volume ratio. Interestingly, the particle size had also an effect on the dissolution rate, which increased with HH initial thickness (Table 2).

Comparing the HH dissolution curve derived from gray value measurements throughout the volume (Figure 4) with the curves obtained for different ranges of particle sizes showed that the kinetics measured globally was close to that observed for small particles (Figure 7 b). This can be explained by the large amount of small particles found in the initial powder, which could not be imaged due to the spatial resolution of the tomograph used in this study. It seemed indeed that very few particles of diameter below 20 µm had begun to dissolve at 1200 s (Figure 7), as confirmed by the incubation times (Table 2). However, the knife setting time of this plaster was equal to 1200 s. This time is known to correspond to the percolation of the gypsum phase in the microstructure, meaning that the

small HH particles (below 20 µm) controlled the initial strengthening of the paste. This first stage could unfortunately not thoroughly be studied in these experimental conditions. Nevertheless, this study shows that the microstructuration of plaster is far from being completed when the knife setting time is reached and that bigger HH particles also play a key role in this evolution.

The granulometry of HH powder had indeed a direct influence on the kinetics of dissolution and precipitation but also on the pore size observed after setting. The comparison of set gypsum prepared from as-received HH powder and HH powder sieved either between 63 and 40 µm or below 40 µm clearly confirmed the strong correlation between HH particles size distribution and mesopore size distribution (Figure 9). This could lead to a possible control of mesopore sizes in the set material. Although the relative density measured for the reference material and for the one obtained after powder sieving was approximately the same, the microstructure of dried plaster obtained with sieved powder was more homogeneous (Figure 8), due to both the decrease of the mesopores size and to the crystallization of thinner or/and better individualized gypsum crystals. Indeed, the gypsum crystals size distribution was wider when as-received HH particles were used (Figure 10b). Such a behavior may be explained by the difference in dissolution times depending on the size of HH powder as emphasized in this work. For a narrow size distribution of small HH particle, the dissolution and subsequent precipitation of gypsum crystals probably occurred over a limited time range, leading to a network of random individualized crystals. For a wide HH size distribution, the dissolution of the smallest particles led to the formation of an initial network of gypsum (controlling the knife setting time). Then, the dissolution of the largest particles released more calcium and sulfate ions leading to additional precipitation of gypsum crystals upon the existing network, as monitored by the *in-situ* observation of the setting. To the best of our knowledge, it is the first time that a study reports and quantifies that the control of the reactant powder size distribution could permit to regulate the thickness and the agglomeration state of the growing gypsum crystals. This appears therefore to be an interesting way of tuning the final mechanical properties of the set plaster [19].

It cannot not be completely ensured that the X-Ray beam had no influence on the setting kinetics of plaster. Nevertheless, the impact on the setting process is likely to be negligible. Thermal effects for example, are probably very small compared to the exothermicity of the setting reaction.

Also, additional work is required to know if, to get an homogeneous microstructure, the determining characteristics of the HH reactive powder is the mean particle size, the width of the particle size distribution, or both.

The results presented in this paper could feed analytical or numerical models of plaster hydration [10,20,21], even if single gypsum crystals could not be individualized due to the resolution used here.

X-Ray computed tomography is becoming a very powerful technique to monitor the microstructuration of setting materials but this type of measurements requires high resolution and low noise images. Both a higher spatial resolution and a quicker acquisition would permit to get more insights into the setting process and especially into the first stages of the process. Fast X-Ray computed tomography experiments could be done using synchrotron, which, owing to the high flux of high-energy X-Ray available, would enable a complete high resolution (1 µm) tomography acquisition to be performed within a few seconds, instead of several minutes.

5. Conclusions

The real time imaging of the plaster setting was carried out for the first time, with a paste rheology close to an industrial one.

The observation of both the dissolution of HH and the formation of a network of gypsum crystals was possible. A critical role played by HH particle size was evidenced: small HH particles were rapidly dissolved, whereas large particles were still not completely dissolved long after the material had started to set. It was also shown that the final dissolution of the largest particles led to the

formation of mesopores in the hydrated material. To our knowledge, this is the first time that the origin of the presence of such mesopores in set plaster is provided, thanks to *in-situ* experiments.

3D image analysis was performed to obtain quantitative information both on a local scale (selected particles) and on a global scale (whole volume). A local dissolution front speed ranging from 1.5 µm/min for large particles to 0.8 µm/min for small ones and a degree of setting reaction based on microstructural evolution were computed. These data could be used in a future study for comparison with the chemical degree of reaction and the development of strength during setting.

Another clear outcome of this study is the evidence of the possibility to play on the morphology of the set material by the granulometry of the starting powder, in order to target better mechanical properties at a similar porosity.

References

[1] A.J. Lewry, J. Williamson, The Setting of Gypsum Plaster: Part I The Hydration of Calcium Sulphate Hemihydrate, J. Mater. Sci. 29 (1994) 5279-5284.

[2] L. Amathieu, R. Boistelle, Crystallization kinetics of gypsum from dense suspension of hemihydrate in water, J. Cryst. Growth. 88 (1998) 183-192.

[3] C. Solberg, S. Hansen, Dissolution of CaSO4 center dot 1/2H(2)O and precipitation of CaSO4 center dot 2H(2)O - A kinetic study by synchrotron X-ray powder diffraction, Cement Concrete Res. 31 (2001) 641-646.

[4] K.M. Song, J. Mitchell, et al., Magnetic resonance studies of hydration kinetics and microstructural evolution in plaster pastes, J. Mater. Sci. 44 (2009) 5004-5012.

[5] Q.L. Yu, H.J.H Brouwers, A.C.J. Korte, Gypsum Hydration: a Theoritical and Experimental Study, In: 17th International Conference on Building Materials, ibausil, Weimar, Germany; 2009.

[6] E. Finot, E. Lesniewska, et al., Investigations of surface forces between gypsum crystals in electrolytic solutions using microcantilevers, J. Chem. Phys. 111 (1999) 6590-6598.

[7] E. Finot, E. Lesniewska, et al., Correlating surface forces with surface reactivity of gypsum crystals by atomic force microscopy. Comparison with theological properties of plaster, Solid State Ionics 141 (2001) 39-46.

[8] M.J. Ridge, Crystal growth in gypsum plaster setting, Aust. J. Appl. Sci. 9 (1958) 163-169.

[9] A.J. Lewry, J. Williamson, The Setting of Gypsum Plaster: Part II The development of Microstructure and Strength, J. Mater. Sci. 29 (1994) 5524-5528.

[10] D.P. Bentz, S. Mizell, et al., The Visible Cement Data Set, J. Res. Natl. Inst. Stan. 107 (2002) 137-148.

[11] A. Bouterf, S. Roux, et al., Digital volume correlation applied to X-Ray tomography images from spherical indentation tests on lightweight gypsum, Strain 50 (2014) 444-453.

[12] E, Gallucci, K. Scrivener, et al., 3D experimental investigation of the microstructure of cement

711 pastes using synchrotron X-ray microtomography (μCT), Cement Concrete Res. 37 (2007) 360-
712 368.
713 [13] J.Y. Buffiere, E. Maire, et al., In Situ Experiments with X ray Tomography: An Attractive Tool
714 for Experimental Mechanics, Exp. Mech. 50 (2010) 289-305.
715 [14] M. Abramoff, P. Magalhaes, et al., Image processing with ImageJ, J. Biophotonics Int. 11
716 (2004) 36-42.
717 [15] J. Schindelin, I. Arganda-Carreras, et al., Fiji: an open-source platform for biological-image
718 analysis, Nat. Methods 9 (2012) 676-682.
719 [16] E. Maire, P. Colombo, et al., Characterization of the morphology of cellular ceramics by 3D
720 image processing of X-Ray tomography, J. Eur. Ceram. Soc. 11 (2004) 36-42.
721 [17] S. Meille, M. Saadaoui, et al., Mechanisms of crack propagation in dry plaster, J. Eur. Ceram.
722 Soc. 23 (2003) 3015-3112.
723 [18] E. M. Gartner, Cohesion and expansion in polycrystalline solids formed by hydration reactions
724 – The case of gypsum plasters, Cement Concrete Res. 39 (2009) 289-295.
725 [19] S. Meille, E.J. Garboczi, Linear elastic properties of 2D and 3D models of porous materials
726 made from elongated objects, Model. Simul. Mater. Sc. 9 (2001) 371-390.
727 [20] G. Dumazer, V. Narayan, et al., Modeling Gypsum Crystallization on a Submicrometric Scale,
728 J. Phys. Chem. C 113 (2009) 1189-1195.
729 [21] A. Lemarchand, F. Boudoire, et al., Plaster Hydration at Different Plaster-to-Water Ratios:
730 Acoustic Emission and 3-Dimensional Submicrometric Simulations, J. Phys. Chem. C 116 (2012)
731 4671-4678.
732
733
734
735

Figure Captions

1. Microstructural changes during the setting of plaster. Reconstructed 2D slices extracted from the 3D volumes acquired during the *in-situ* tomography experiments, between 800 and 3000 seconds. The last slice (24h) was obtained after drying at 45°C.

2. 3D rendering of a) HH particle (800 s), length = 123 µm b) Resulting mesopore after setting and drying (24 h), length = 113 µm.

3. Histograms of the gray values measured in the volumes for different times during setting and then subsequent drying at 45°C.

4. Evolution of the intensity of the HH peak (dashed line in Figure 3, gray level value = 0.31) and of the gypsum peak (dashed line in Figure 3, gray level value = 0.21).

5. Gray values profile along the red line taken at different setting times. The measurement was focused on a small HH particle (20 µm thick).

6. Gray values profile along the red line taken at different setting times. The measurement was focused on a large HH particle (70 µm thick).

7. a) HH thickness evolution during setting for different classes of initial particle sizes b) Normalized thickness evolution of HH particles (solid lines). The dashed line corresponds to the average HH dissolution throughout the whole volume as measured from data of Figure 4 (evolution of normalized intensity of HH gray value peak).

8. Reconstructed 2D slices extracted from 3D volumes of set plaster samples obtained with a) the as-received HH powder and b) HH powder sieved below 40 µm – voxel size of 2.5 μm^3 and set plasters samples prepared with c) as-received powder and d) powder sieved below 40 µm – voxel size of 0.4 μm^3.

9. Size distribution of mesopores in set plaster for different HH granulometry. « Reference » for sample prepared with as-received HH powder, « < 40 µm » for HH sieved below 40 µm.

10. Granulometry of the porous « phase » (a) and of the gypsum phase (b) measured from high resolution acquisitions (0.4 μm^3 voxel size).

11. Schematic representation of the hydration process as monitored by X-Ray tomographic observation (blue : water ; black : entrapped air ; white : HH particles of typical size between a few µm and tens of µm ; gray : DH crystals).

Supplementary Online Materials

Video 1: time lapse movie of plaster setting